Chemical Science

ROYAL SOCIETY OF CHEMISTRY

EDGE ARTICLE

View Article Online
View Journal

Check for updates

Cite this: DOI: 10.1039/d5sc09306f

All publication charges for this article have been paid for by the Royal Society of Chemistry

Received 28th November 2025
Accepted 5th April 2026

DOI: 10.1039/d5sc09306f

rsc.li/chemical-science

Regulating KBBF-like structures *via* a charge-assisted hydrogen-bonded framework to enable easily grown ultraviolet nonlinear optical crystals

Mingshu Zhang, [a] Shuya Zhao,[a] Zhen-Cheng Wu,[b] Yue Yin,[a] Zheyu Zhang,[a] Jiafeng Chen,[a] Sheng-Ping Guo *[b] and Yan Zhou *[a]

Growing large, high-quality nonlinear optical (NLO) crystals remains a central challenge for advancing ultraviolet (UV) laser technologies. $KBe_2BO_3F_2$ (KBBF)-type crystals exhibit outstanding NLO properties but suffer from pronounced layer separation that impedes the growth of application-scale single crystals. Here, we introduce a three-dimensional (3D) charge-assisted hydrogen-bonded framework strategy by incorporating sulfanilamide and nitrate anions as hydrogen-bond donors and acceptors into a KBBF-like structure. This approach led to the successful synthesis of a novel ultraviolet (UV) NLO crystal, $C_6H_9N_2SO_2\cdot NO_3$ (SAN), which preserves a KBBF-like architecture while being stabilized by an extensive hydrogen-bonding network. SAN demonstrates a stronger second-harmonic generation (SHG) response (2.5 × KH_2PO_4, KDP) and higher birefringence (0.112 at 546 nm) compared with KBBF. Crucially, the 3D hydrogen-bonded network suppresses layer exfoliation and enables direct growth of centimeter-scale crystals (4.5 × 1 × 0.5 cm^3) from aqueous solution by simple evaporation at room temperature. This work pioneers the integration of hydrogen-bonded framework design into the structural modification of NLO crystals. Through rational hydrogen-bond engineering within the KBBF-type framework, the crystal growth behavior has been significantly improved, establishing a generalizable strategy for modifying other layered functional crystalline materials.

Introduction

Nonlinear optical (NLO) crystals are indispensable for frequency conversion beyond intrinsic laser gain bandwidths, enabling coherent radiation in the ultraviolet (UV) and deep-UV regions for high-resolution lithography, photochemistry, and ultrafast science.[1–13] Workhorse UV NLO crystals such as LiB_3O_5 (LBO), β-BaB_2O_4 (BBO), and KH_2PO_4 (KDP), together with $KBe_2BO_3F_2$ (KBBF),[14–17] have propelled the development of UV photonics over the past few decades. Among them, KBBF stands out for deep-UV second-harmonic generation (SHG), yet its practical deployment is severely constrained by toxic precursors and the intrinsic tendency toward layered growth, which complicates the growth of thick and crack-free single crystals suitable for device integration.[18] In response, considerable research has been devoted to structural modification and compositional engineering aimed at overcoming these inherent limitations of KBBF and developing viable alternatives, leading to a number of important advances: compositional substitution of the toxic $[BeO_3F]$ groups and the introduction of interlayer covalent linkages have produced KBBF-family derivatives like $Zn_2BO_3(OH)$, $NaZnCO_3(OH)$, β-$Rb_2Al_2B_2O_7$, and $(NH_4)_3B_{11}PO_{19}F_3$,[19–22] with reduced interlayer spacing while retaining appreciable NLO responses. Beyond covalent interlayer bridging, alternative strategies have been explored to constrain interlayer separation *via* hydrogen-bonding interactions, as demonstrated in $NH_4B_4O_6F$, $NH_4Be_2BO_3F_2$, $C(NH_2)_3SO_3F$ and $[C_2N_4H_7O][NH_2SO_3]$.[23–26] Nonetheless, the growth of large single crystals remains challenging for most KBBF-family compounds, with even millimeter-sized crystals often exhibiting pronounced lamellar morphology due to incomplete suppression of anisotropic growth. Therefore, a more effective strategy is needed to strengthen interlayer cohesion without sacrificing NLO performance.

Hydrogen-bonded organic frameworks (HOFs) provide a promising blueprint.[27,28] As an emerging class of crystalline porous materials, HOFs have undergone rapid development in recent years and been extensively applied in cutting-edge fields including gas adsorption/separation, proton conduction, and catalysis.[29–31] The self-assembly *via* intermolecular hydrogen bonding endows these materials with high crystallinity and excellent solution processability.[32,33] Moreover, the abundant hydrogen-bonding interactions in HOFs can effectively establish well-defined 3D frameworks. These characteristics provide

---

[a] *School of Chemical Science and Technology, Yunnan University, Kunming, Yunnan 650500, P. R. China. E-mail: yanzhou@ynu.edu.cn*

[b] *Yunnan Key Laboratory of Electromagnetic Materials and Devices, School of Materials and Energy, Yunnan University, Kunming, Yunnan 650500, P. R. China. E-mail: spguo@ynu.edu.cn*

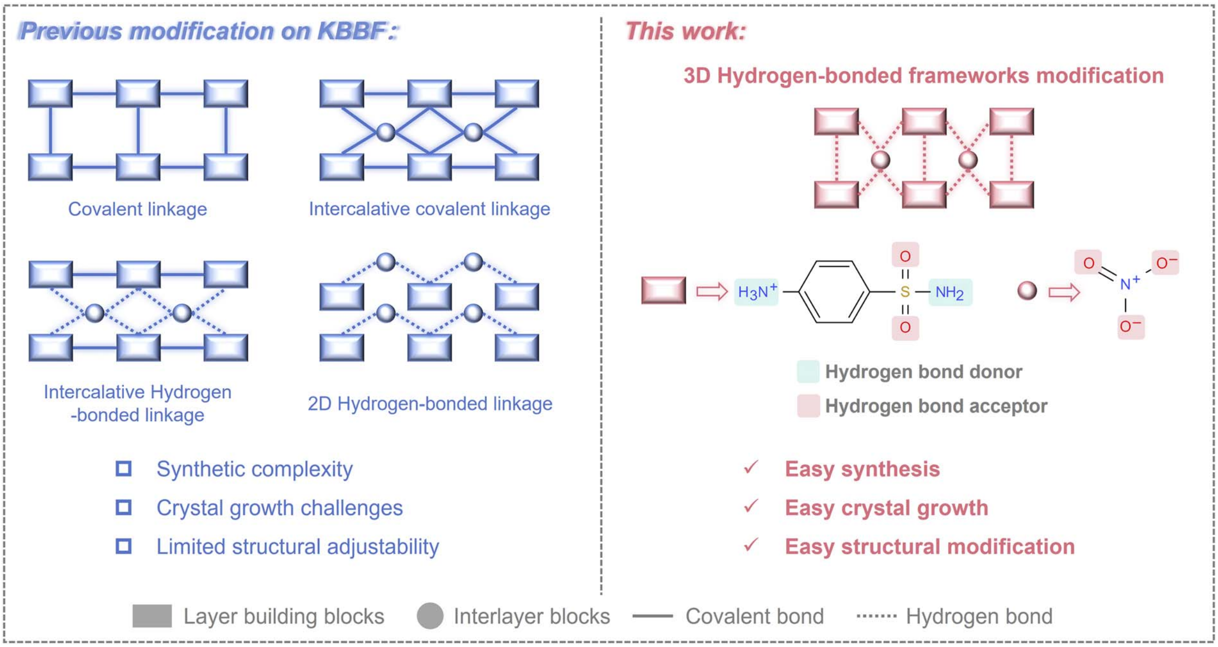

Fig. 1 Schematic of modification strategies for KBBF-type crystals in previous studies and this work.

valuable insights for addressing the inherent crystal growth issues in KBBF-type structures. Specifically, replacing the structural units of KBBF with functional groups that feature rich hydrogen-bonding environments is anticipated to facilitate the formation of 3D architectures. However, the relatively weak nature of hydrogen bonds poses challenges to structural stability. Strengthening intermolecular interactions through charge-assisted hydrogen bonding by integrating paired acids and bases would be a more optimal strategy, as such electrostatically enhanced interactions can significantly improve structural robustness while maintaining framework dimensionality.[32,34]

Guided by these considerations, we selected sulfanilamide ($C_6H_8N_2O_2S$) and nitric acid (HNO_3) for combination based on the following rational design considerations (Fig. 1): (i) the $-NH_2$ and $-SO_2NH_2$ groups in sulfanilamide can act as hydrogen bond donors and acceptors, enabling intermolecular hydrogen bonding. Additionally, the nitrate anion serves as an effective hydrogen bond acceptor, further enriching the hydrogen bond network; (ii) as a strong acid, nitric acid can form charge-assisted hydrogen bonds with sulfanilamide, which significantly enhances the structural stability through electrostatically enhanced interactions; (iii) both the benzene ring in sulfanilamide and the nitrate anion are π-conjugated units exhibiting high polarizability anisotropy and hyperpolarizability. Their rational alignment within the framework is conducive to enhancing the SHG response and birefringence. Furthermore, π–π stacking also contributes to the stabilization of the hydrogen-bonded framework. By leveraging these design principles, we successfully constructed a 3D hydrogen-bonded framework structurally analogous to KBBF, leading to the discovery of a novel UV NLO crystal $C_6H_9N_2SO_2\cdot NO_3$ (SAN). As intended, centimeter-sized single crystals of SAN were grown at room temperature *via* simple aqueous solution evaporation, with the largest crystal reaching $4.5 \times 1 \times 0.5$ cm^3 in size. Furthermore, SAN exhibits excellent NLO performance, surpassing KBBF in both SHG efficiency (2.5 × KDP) and birefringence (0.112). This work demonstrates the effectiveness of hydrogen-bonded framework engineering in simultaneously optimizing the structural architecture and crystal growth behavior of UV NLO materials, providing a viable and instructive pathway for future design of such materials.

Results and discussion

The growth of SAN crystals can be readily achieved under laboratory conditions without the need for specialized equipment or elevated temperatures (Fig. 2a). The crystal size demonstrates a dependence on container dimensions, indicating benign growth kinetics. Detailed procedures for crystal synthesis and growth are provided in the SI. To further elucidate the crystallization behavior of SAN, we employed the Bravais–Friedel–Donnay–Harker (BFDH) model to predict its crystal habit. As depicted in Fig. 2b, the simulated crystal morphology of SAN demonstrates a prominent blocky tendency, and there is no significant disparity in the growth rate (*D* value) of each crystal face along the direction perpendicular to the crystal plane (Fig. 2c). This observation suggests relatively low anisotropy in the crystal growth process. Single-crystal X-ray diffraction (SCXRD) and energy-dispersive X-ray spectroscopy (EDS) analysis results confirm the crystal structure and composition (Fig. S1); powder X-ray diffraction (PXRD) results verify phase purity for optical measurements (Fig. S2). SAN crystals are non-hygroscopic and retain integrity after at least six months under ambient conditions.

SAN crystallizes in the non-centrosymmetric space group *Cc* (No. 9, detailed crystallographic information is presented in

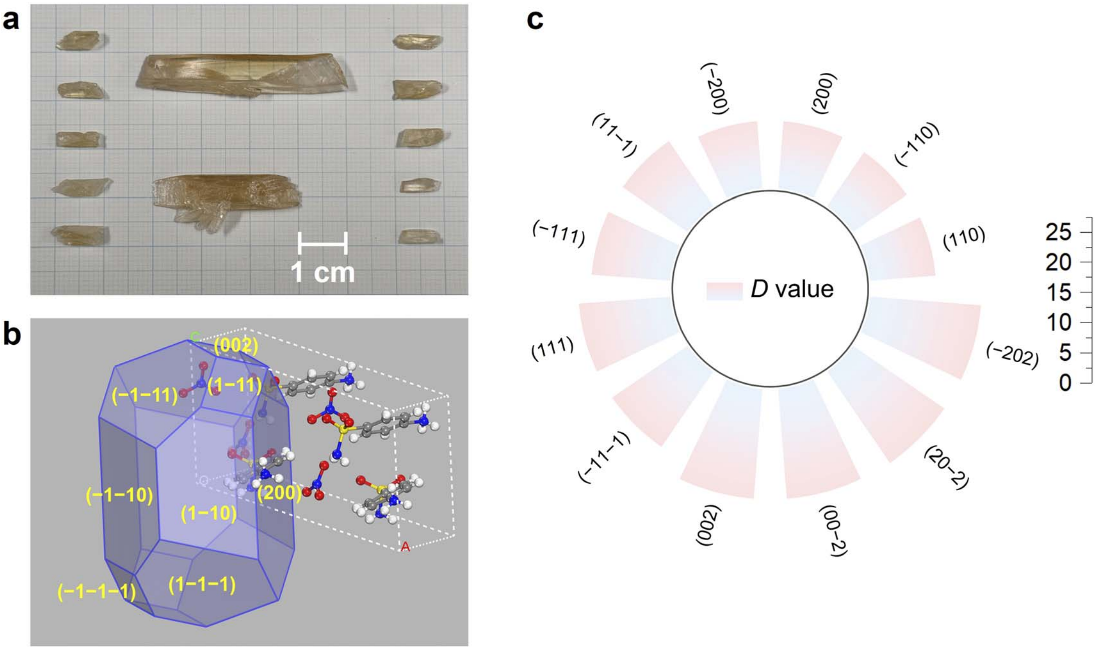

Fig. 2 Photograph of as-grown SAN crystals (a); simulated crystal habit of SAN based on the BFDH model (b); simulated growth rates for individual crystal faces of the SAN crystal (c).

Tables S1 to S3). The asymmetric unit contains one $[C_6H_9N_2O_2S]^+$ cation and one $[NO_3]^-$ anion linked by charge-assisted N–H···O hydrogen bonds. A structural comparison between SAN and KBBF is shown in Fig. 3a and b. In KBBF, the honeycomb-like $[Be_2BO_3F]$ 2D layers are built from $[BeO_3F]$ tetrahedra and $[BO_3]$ triangles (Fig. 3c), with K^+ ions occupying interlayer sites as counterions. The interlayer interactions are dominated by K–F ionic bonds, resulting in a large interlayer spacing and contributing to its pronounced layering tendency. SAN features pseudo-2D layers composed of $[C_6H_9N_2O_2S]^+$

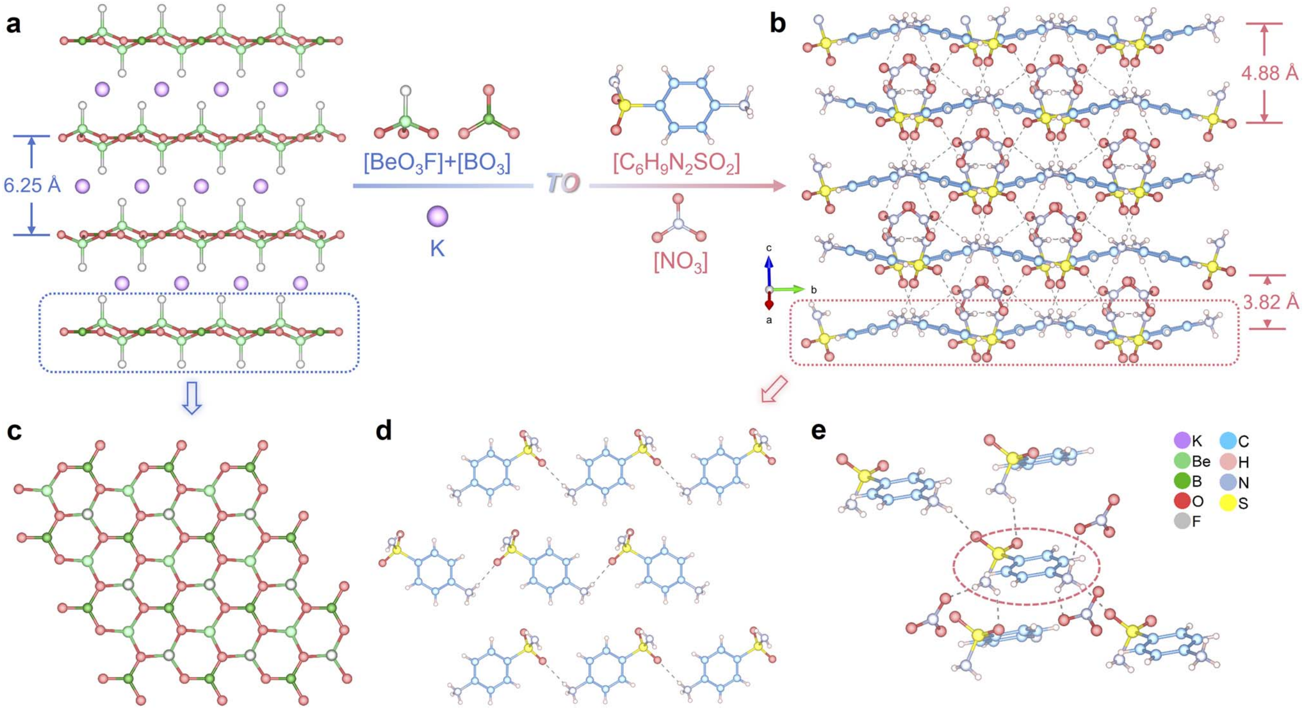

Fig. 3 Structural comparison between KBBF and SAN (a and b); 2D/*pseudo*-2D layers of KBBF (c) and SAN (d); the hydrogen-bonding environment of $[C_6H_9N_2O_2S]^+$ (e).

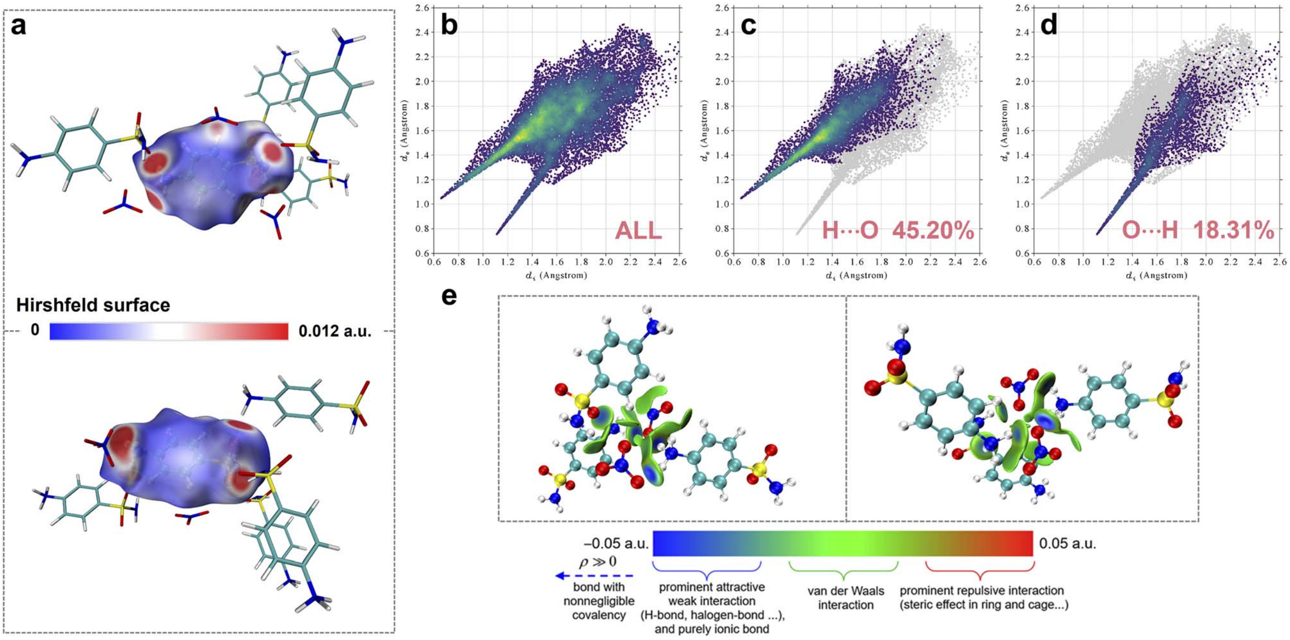

Fig. 4 The Hirshfeld isosurface of SAN in different directions (a); 2D fingerprint plots for overall interactions and individual H···O/O···H interactions in the crystal packing of SAN (b–d); IGMH isosurfaces of SAN in different directions (e).

moieties with $[NO_3]^-$ occupying the interlayer regions (Fig. 3d). Notably, whereas the layers of KBBF are rigid due to extensive covalent bonding, the interlayer forces are weak ionic interactions, leading to strongly anisotropic growth. In contrast, the pseudo-2D layers in SAN are formed by $[C_6H_9N_2O_2S]^+$ with relatively large intermolecular distances and no direct covalent linkages. These groups are interconnected *via* N–H···O hydrogen bonds between the interlayer $[NO_3]^-$ anions. Furthermore, the $[C_6H_9N_2O_2S]^+$ units across neighboring layers are also bridged by hydrogen bonds (Fig. 3e), giving rise to a highly interconnected zigzag layer topology. This extensive hydrogen-bonding network imparts greater structural homogeneity and enhanced dimensional control in SAN, effectively reducing and stabilizing the interlayer spacing. The maximum and minimum interlayer distances in SAN are 4.88 Å and 3.82 Å, respectively, both significantly smaller than the interlayer spacing in KBBF (6.25 Å).

To gain deeper insights into the intermolecular interactions, a Hirshfeld surface analysis was performed on SAN.[35–37] As illustrated in Fig. 4a, prominent hydrogen-bonding interactions are observed within the crystal structure. Specifically, the protonated amino group of $[C_6H_9N_2O_2S]^+$ engages in strong N–H···O hydrogen bonds with both the neighboring $-SO_2NH_2$ and $[NO_3]^-$. Moreover, weak C–H···O contacts exist between aromatic hydrogen atoms and $[NO_3]^-$. Fingerprint plots and quantitative analyses of contact contributions derived from the Hirshfeld surface reveal that hydrogen bonds involving oxygen as an acceptor account for 63.5% of all intermolecular contacts in SAN, underscoring the dominant role of O-centered hydrogen bonding in constructing the architecture of SAN (Fig. 4b to d). The independent gradient model based on Hirshfeld partition (IGMH) isosurfaces further map the spatial distribution of these interactions (Fig. 4e),[38,39] corroborating the pervasive hydrogen-bonding network responsible for the 3D framework.

The ultraviolet–visible–near-infrared (UV-Vis-NIR) transmission spectrum of millimeter-scale SAN single crystals reveals that its absorption edge extends into the solar blind region, with a cut-off wavelength at 272 nm (Fig. 5a and S3), corresponding to an optical bandgap of 4.56 eV. Furthermore, the measured crystal maintains a transmittance exceeding 90% across the broad spectral range of 300–2500 nm, demonstrating excellent optical transparency and high crystalline quality. Therefore, SAN emerges as a promising candidate for 355 nm Nd:YAG sum frequency generation as well as other UV applications spanning the 300–400 nm range. The structural modification from KBBF to SAN entails the substitution of functional groups with extended π-conjugated modules, which strengthens the π–π* interactions. Such enhanced electronic delocalization leads to a narrowing of the band gap, consequently inducing a redshift in the UV cut-off edge of SAN compared to that of KBBF. The infrared spectrum of SAN is presented in Fig. S4. The N–H stretching vibration displays distinct red-shift and broadening features, whereas the antisymmetric and symmetric stretching vibrations of S═O exhibit an overall shift toward lower wavenumbers with intense peak characteristics. These observations indicate the presence of relatively strong N–H···O(SO_2) interactions, which is consistent with the charge-assisted hydrogen bond model. The thermal behavior of SAN was systematically examined through thermogravimetric (TG) and derivative thermogravimetric (DTG) analyses (Fig. 5b). SAN remains thermally stable up to approximately 190 °C, beyond which three successive mass-loss stages occur, culminating in a total weight loss of about 69.5% and leaving a residual mass of roughly 30% at 800 °C. The first decomposition stage, centered at 192 °C and corresponding to a 23.1% mass reduction, is attributed

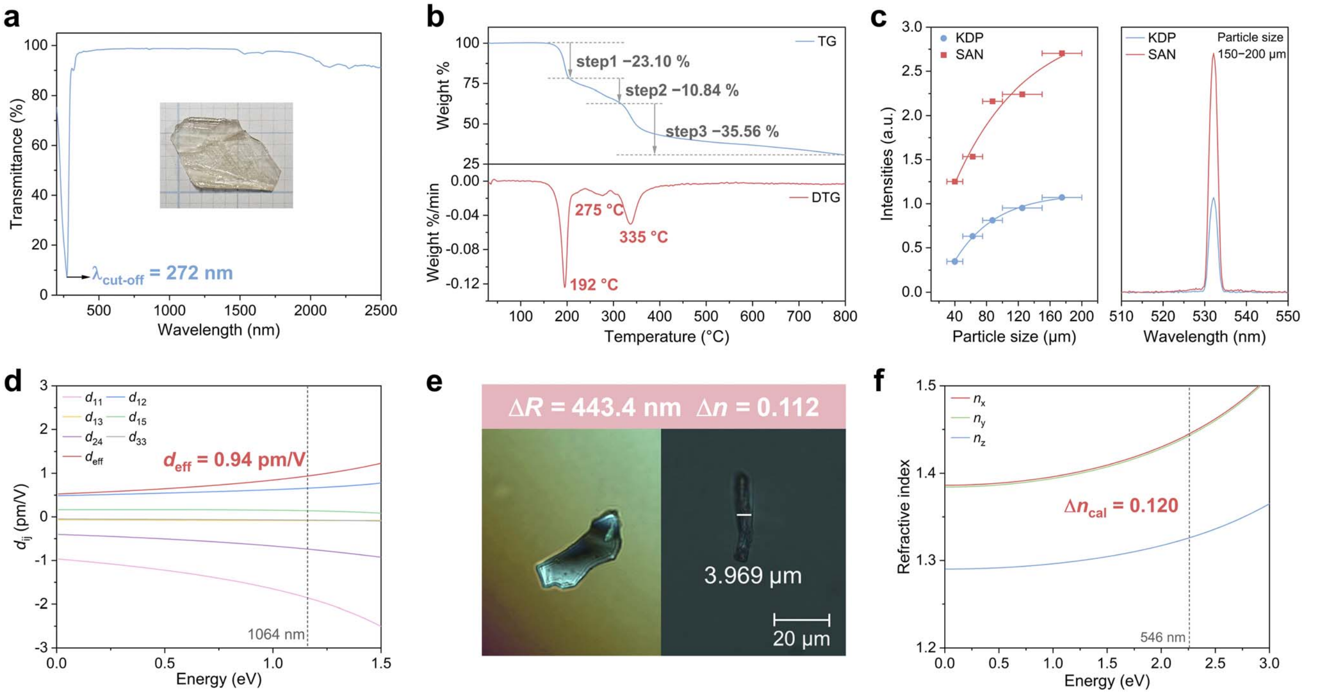

Fig. 5 The UV–Vis–NIR transmission spectrum of millimeter-scale SAN single crystals with a thickness less than 1 mm (a); TG and DTG curves (b); phase-matching curve and SHG intensity (c); theoretical SHG coefficient (d); experimental birefringence measurements (e); and theoretical birefringence (f) of SAN.

primarily to the denitration or partial decomposition of the $[NO_3]^-$ moiety. The experimental mass loss closely approximates the theoretical nitrate content (26.4%), suggesting the liberation of nitrogen oxides. The second stage, occurring near 275 °C with a 10.84% mass loss, likely involves further decomposition of nitrogen-containing intermediates and partial cleavage of the sulfonamide linkage. The third decomposition event, centered at 335 °C with a 35.56% weight loss, corresponds to the breakdown of the organic framework, including fragmentation of the carbon skeleton and sulfur oxidation, resulting in the evolution of SO_x and hydrocarbon species. Collectively, these results demonstrate that SAN exhibits good thermal stability up to 192 °C, which exceeds that of several recently reported NLO crystals where hydrogen bonding serves as the primary linking interaction, including $SbF_3\cdot Gly$ (105 °C), $O_3SCH_2NH_3$ (187 °C), $[CN_3H_6][C_3H_3O_4]$ (157 °C), $(C_5H_6ON)^+(H_2PO_4)^-$ (166 °C), and $KNO_3SO_3NH_3$ (140 °C).[40–44]

Since SAN crystallizes in a non-centrosymmetric space group, its particle-size-dependent SHG response was systematically investigated under 1064 nm laser irradiation. As shown in Fig. 5c, the SHG intensity of SAN increases with increasing particle size, consistent with phase-matching behavior. At particle sizes ranging from 150–200 μm, the SHG intensity of SAN reaches 2.5 times that of KDP of comparable dimensions, outperforming its parent compound KBBF (1.2 × KDP)[18] and comparable to several recently reported excellent UV NLO crystals, such as $La_3Ga_3Ge_2S_3O_{10}$ (2 × KDP), $Rb_3PbBi(P_2O_7)_2$ (2.8 × KDP) and $Mg(C_3O_4H_2)(H_2O)_2$ (3 × KDP).[45–47] We also investigated the NLO properties of SAN using theoretical methods (Fig. 5d). SAN crystallizes in the point group m, with six non-zero SHG coefficients d_{11}, d_{12}, d_{13}, d_{15}, d_{24} and d_{33}. The calculated SHG coefficients at 1064 nm are −1.87, 0.66, −0.08, 0.14, −0.72 and −0.07 pm V^{-1}, respectively, yielding an effective SHG coefficient d_{eff} of 0.94 pm V^{-1}, which is approximately 2.4 times that of KDP (0.39 pm V^{-1}). This result is in excellent agreement with experimental results. To further explore the origin of the NLO properties, we performed a group-resolved analysis to evaluate the contribution of individual structural units. The analysis reveals that the $[C_6H_9N_2O_2S]^+$ group dominates the contributions to all SHG coefficients in SAN (Fig. S5). It is well established that the macroscopic NLO performance of a crystal depends not only on the intrinsic properties of its functional groups but also critically on their spatial arrangement within the structure. The hyperpolarizability of the $[C_6H_9N_2O_2S]^+$ group was visualized using the unit-sphere representation method,[48] revealing that its resultant vector lies coplanar with the benzene ring and is directed toward the sulfonamide moiety (Fig. S6a). Furthermore, the individual hyperpolarizability contributions from the $[C_6H_9N_2O_2S]^+$ groups are orthogonally aligned along the c-axis, resulting in a coherent macroscopic polarization (Fig. S6b). This well-ordered spatial arrangement significantly enhances the overall SHG response of SAN.

The birefringence of SAN was experimentally determined using a polarizing microscope with a 546 nm light source (Fig. 5e). The thickness (T) of the measured crystal was 3.969 μm, and the corresponding optical path difference (ΔR) was found to be 443.4 nm. By applying the formula $\Delta R = \Delta n \times T$, the experimental birefringence Δn_{exp} was derived as 0.112, which exceeds that of KBBF (0.077) and several members of the KBBF family,[18] such as $K_{15}La_7(BO_3)_{12}$ (0.065), $Rb_3B_{11}P_2O_{23}$ (0.071) and

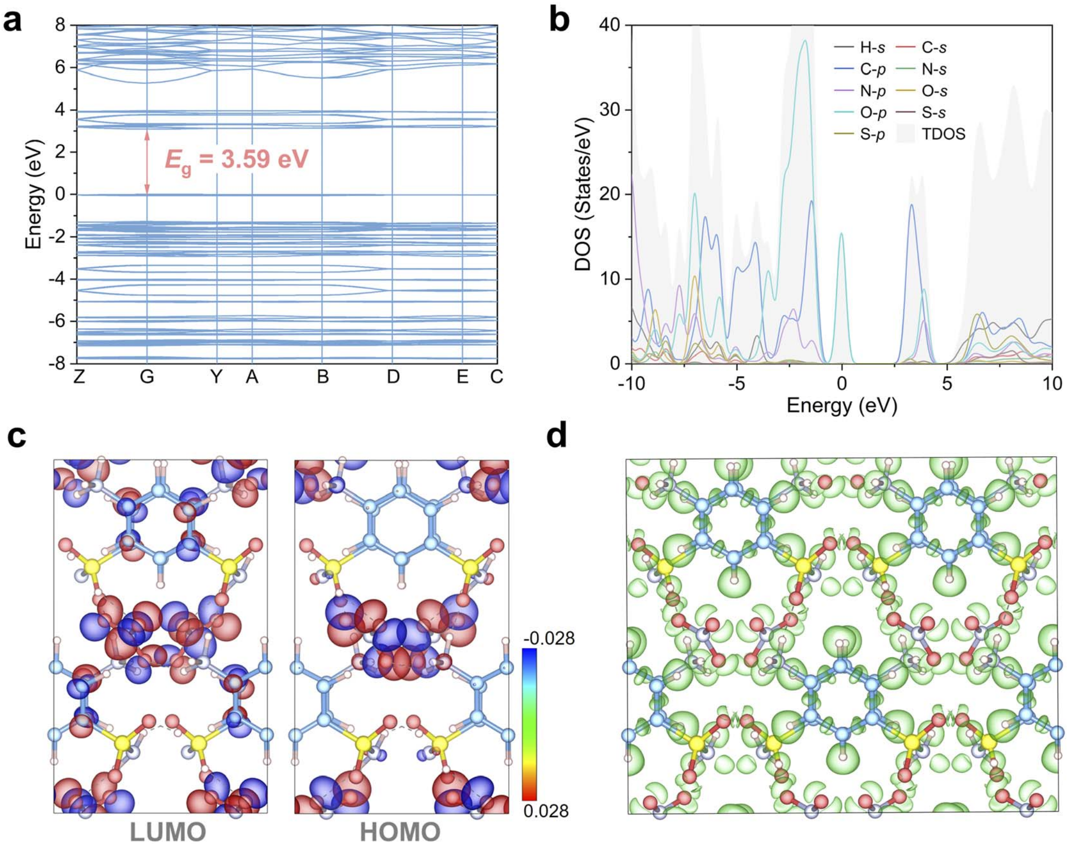

Fig. 6 The electronic band structure (a); DOS (b); HOMO–LUMO isosurface (c); and 3D ELF map (d) of SAN.

KLi_2CO_3F (0.102).[49–51] The enhanced birefringence enables materials to achieve an equivalent optical path difference over a reduced physical length, thereby offering significant advantages for the design of integrated optical systems and the development of miniaturized photonic devices. The augmented birefringence of SAN can be ascribed to the substitution of $[BeO_3F]$ and $[BO_3]$ units with the $[C_6H_9N_2O_2S]$ group in SAN. The latter exhibits a markedly higher polarizability anisotropy (58.99) compared to 17.76 for $[BeO_3F]$ and 14.97 for $[BO_3]$, thereby significantly boosting the overall birefringence response. First-principles calculations were performed to investigate the birefringence of SAN. SAN crystallizes in the monoclinic system and belongs to the biaxial crystal system, with three principal refractive indices designated as n_x, n_y, and n_z. These refractive indices follow the order $n_x > n_y > n_z$. As a result, the theoretical birefringence at 546 nm, defined as $\Delta n_{\mathrm{cal}} = n_x - n_z$, is computed to be 0.120, in good agreement with the experimental value (Fig. 5f). Based on the refractive index dispersion, we further calculated the phase-matching cutoff edge of SAN (Fig. S7). The results demonstrate that the phase-matching cutoff edge of SAN is 650 nm, which is consistent with the experimentally observed phase-matching behavior.

The electronic structure of SAN was computed to gain a more profound understanding of its structure–property relationship. As depicted in Fig. 6a, SAN is identified as a direct-bandgap semiconductor, with a theoretical bandgap of 3.59 eV. The deviation between the theoretical and experimental values can be ascribed to the intrinsic derivative discontinuity flaw of the GGA-PBE functional. Analyzing the density of states (DOS) of SAN reveals that near the Fermi level, the electronic states are predominantly occupied by C-2p, O-2p and N-2p orbitals (Fig. 6b). This finding suggests that the optical properties of SAN are chiefly governed by the $[C_6H_9N_2O_2S]^+$ and $[NO_3]^-$ groups. We performed a visualization of the highest occupied molecular orbital (HOMO) and the lowest unoccupied molecular orbital (LUMO) within a unit cell of SAN to elucidate their distributions. As shown in Fig. 6c, the HOMO is primarily localized on the $[NO_3]^-$ group, whereas the LUMO displays a notable distribution in both $[C_6H_9N_2O_2S]^+$ and $[NO_3]^-$ moieties, indicating intermolecular charge transfer characteristics in SAN. The interaction between $[C_6H_9N_2O_2S]^+$ and $[NO_3]^-$ groups is essentially dominated by hydrogen bonds driven by electrostatic forces, rather than electronic delocalization or sharing, which aligns with our expectations. To further probe the electronic structure, we conducted a 3D electron localization function (ELF) analysis (Fig. 6d). The resulting isosurface maps reveal highly anisotropic electron distribution patterns centered on the $[C_6H_9N_2O_2S]^+$ and $[NO_3]^-$ groups, providing a clear electronic basis for the enhanced SHG response and birefringence observed in SAN relative to KBBF. Moreover, regions of high electron localization are clearly observed at both hydrogen bond donors and acceptors, confirming that the hydrogen bond network in SAN is reinforced through substantial charge polarization, thereby optimizing structural stability and crystal growth habit.

Conclusions

In summary, we have successfully developed a novel UV NLO crystal, $C_6H_9N_2SO_2 \cdot NO_3$ (SAN), by incorporating a 3D charge-assisted hydrogen-bonded framework into a KBBF-like structural architecture. This strategy effectively overcomes the layer-separation issue inherent in KBBF and its derivatives, enabling the facile growth of large single crystals (up to 4.5 × 1 × 0.5 cm^3) directly from aqueous solution at room temperature. SAN exhibits excellent NLO performance, including a short UV cut-off edge (272 nm), strong SHG (2.5 × KDP) and large birefringence (0.112 at 546 nm). Theoretical calculations corroborate the experimental results and reveal that the optimized alignment of $[C_6H_9N_2O_2S]^+$ cations within the framework is responsible for the enhanced optical properties. This work demonstrates the great potential of hydrogen-bonded framework engineering as a general and effective strategy for modifying layered functional crystals. By rationally introducing charge-assisted hydrogen bonds, we have simultaneously improved crystal growth behavior and optical performance, paving the way for the development of next-generation UV NLO materials.

Author contributions

Mingshu Zhang: conceptualization, visualization, writing-original draft; Shuya Zhao: data curation; Zhen-Cheng Wu: data curation; Yue Yin: data curation; Zheyu Zhang: data curation; Jiafeng Chen: data curation; Sheng-Ping Guo: writing–review & editing, funding acquisition; Yan Zhou: writing–review & editing, funding acquisition, supervision.

Conflicts of interest

There are no conflicts to declare.

Data availability

The data supporting this article have been included as part of the supplementary information (SI). Supplementary information is available. See DOI: https://doi.org/10.1039/d5sc09306f.

Acknowledgements

This work was supported by National Natural Science Foundation of China (22401245 and 22371246), Yunnan Fundamental Research Projects (202401AS070120) and the Yunnan University Undergraduate Innovation Training Program Project (20251091).

Notes and references

1 X. Dong, L. Huang and G. Zou, *Acc. Chem. Res.*, 2025, **58**, 150–162.
2 G. Zou and K. M. Ok, *Chem. Sci.*, 2020, **11**, 5404–5409.
3 C. Wu, G. Yang, M. G. Humphrey and C. Zhang, *Coord. Chem. Rev.*, 2018, **375**, 459–488.
4 W. Zhou and S.-P. Guo, *Acc. Chem. Res.*, 2024, **57**, 648–660.
5 M. Mutailipu, J. Han, Z. Li, F. Li, J. Li, F. Zhang, X. Long, Z. Yang and S. Pan, *Nat. Photonics*, 2023, **17**, 694–701.
6 W. Zeng, J. Zhang, Y. Tian, H. Zeng, Z. Lin, L. Zhou, K. M. Ok and G. Zou, *Angew. Chem., Int. Ed.*, 2025, **65**, e20861.
7 C. C. Jin, Y. Li, J. S. Kim, J.-H. Lim, H. Huang, C.-A. Chen, J. Lee, Y. Heo, B. Zhang, J. I. Jang and K. M. Ok, *Angew. Chem., Int. Ed.*, 2025, **64**, e202512618.
8 Y. Kang, C. Yang, J. Gou, Y. Zhu, Q. Zhu, W. Xu and Q. Wu, *Angew. Chem., Int. Ed.*, 2024, **63**, e202402086.
9 X. Zhang, X. Jiang, H. Gao, K. Duanmu, C. Wu, Z. Lin, Z. Huang, M. G. Humphrey and C. Zhang, *Angew. Chem., Int. Ed.*, 2025, e202513438.
10 H. Tian, C. Lin, Y. Zhou, X. Zhao, H. Fan, T. Yan, N. Ye and M. Luo, *Angew. Chem., Int. Ed.*, 2023, **62**, e202304858.
11 Y. Zhu, J. Gou, C. Yang, Q. Zhu, Y. Xiong and Q. Wu, *Angew. Chem., Int. Ed.*, 2025, **64**, e202509290.
12 C. Wu, X. Jiang, Z. Wang, H. Sha, Z. Lin, Z. Huang, X. Long, M. G. Humphrey and C. Zhang, *Angew. Chem., Int. Ed.*, 2021, **60**, 14806–14810.
13 Y. Yan, X. Wen, P. Tang, J. Lu, J. Chen, J. Wang, Z. Hu, N. Ye and G. Peng, *Angew. Chem., Int. Ed.*, 2025, **64**, e202516953.
14 C. Chen, Y. Wu, A. Jiang, B. Wu, G. You, R. Li and S. Lin, *J. Opt. Soc. Am. B*, 1989, **6**, 616–621.
15 C. Chen, B. Wu, A. Jiang and G. You, *Sci. China, Ser. B*, 1985, **28**, 235–243.
16 J. J. De Yoreo, A. K. Burnham and P. K. Whitman, *Int. Mater. Rev.*, 2002, **47**, 113–152.
17 D. Cyranoski, *Nature*, 2009, **457**, 953–955.
18 C. T. Chen, G. L. Wang, X. Y. Wang and Z. Y. Xu, *Appl. Phys. B*, 2009, **97**, 9–25.
19 X. Wang, F. Zhang, L. Gao, Z. Yang and S. Pan, *Adv. Sci.*, 2019, **6**, 1901679.
20 G. Peng, C. Lin and N. Ye, *J. Am. Chem. Soc.*, 2020, **142**, 20542–20546.
21 T. T. Tran, N. Z. Koocher, J. M. Rondinelli and P. S. Halasyamani, *Angew. Chem., Int. Ed.*, 2017, **56**, 2969–2973.
22 B. Cheng, Z. Li, Y. Chu, A. Tudi, M. Mutailipu, F. Zhang, Z. Yang and S. Pan, *Natl. Sci. Rev.*, 2022, **9**, nwac110.
23 G. Shi, Y. Wang, F. Zhang, B. Zhang, Z. Yang, X. Hou, S. Pan and K. R. Poeppelmeier, *J. Am. Chem. Soc.*, 2017, **139**, 10645–10648.
24 G. Peng, N. Ye, Z. Lin, L. Kang, S. Pan, M. Zhang, C. Lin, X. Long, M. Luo, Y. Chen, Y.-H. Tang, F. Xu and T. Yan, *Angew. Chem., Int. Ed.*, 2018, **57**, 8968–8972.
25 M. Luo, C. Lin, D. Lin and N. Ye, *Angew. Chem., Int. Ed.*, 2020, **59**, 15978–15981.

26 X. Wen, Y. Yan, J. Lu, X. Shi, P. Tang, J. Chen, G. Yang, G. Peng, H. Yu, H. Zhang, Z. Hu, J. Wang and N. Ye, *Angew. Chem., Int. Ed.*, 2025, **64**, e202424153.

27 H. Ali, B. A. Alwan, A. Abdulrahman, D. Yue and A. Hayat, *Mater. Today*, 2025, **88**, 783–813.

28 R.-B. Lin and B. Chen, *Chem*, 2022, **8**, 2114–2135.

29 A. Ebadi Amooghin, H. Sanaeepur, M. Ghomi, R. Luque, H. Garcia and B. Chen, *Coord. Chem. Rev.*, 2024, **505**, 215660.

30 Y. Sun, J. Wei, Z. Fu, M. Zhang, S. Zhao, G. Xu, C. Li, J. Zhang and T. Zhou, *Adv. Mater.*, 2023, **35**, 2208625.

31 H. Yuan, J. Xiao, A.-A. Zhang, Z.-B. Fang and T.-F. Liu, *EnergyChem*, 2025, **7**, 100151.

32 X. Song, Y. Wang, C. Wang, D. Wang, G. Zhuang, K. O. Kirlikovali, P. Li and O. K. Farha, *J. Am. Chem. Soc.*, 2022, **144**, 10663–10687.

33 B. Wang, R.-B. Lin, Z. Zhang, S. Xiang and B. Chen, *J. Am. Chem. Soc.*, 2020, **142**, 14399–14416.

34 X.-Y. Chen, L.-H. Cao, X.-T. Bai and X.-J. Cao, *Chem.–Eur. J.*, 2024, **30**, e202303580.

35 M. A. Spackman and D. Jayatilaka, *CrystEngComm*, 2009, **11**, 19–32.

36 T. Lu and F. Chen, *J. Comput. Chem.*, 2012, **33**, 580–592.

37 T. Lu, *J. Chem. Phys.*, 2024, **161**, 082503.

38 T. Lu and Q. Chen, *J. Comput. Chem.*, 2022, **43**, 539–555.

39 T. Lu, *Angew. Chem., Int. Ed.*, 2025, **64**, e202504895.

40 Z. Bai, J. Lee, C.-L. Hu, G. Zou and K. M. Ok, *Chem. Sci.*, 2024, **15**, 6572–6576.

41 Z. Wang, X. Jiang, X. Wang, K. Duanmu, L. Bai, C. Wu, Z. Lin, Z. Huang, M. G. Humphrey and C. Zhang, *J. Am. Chem. Soc.*, 2026, **148**, 135–140.

42 Z. Chen, C. Liu, C. Li, J. Lu, Z. Yang, S. Pan and M. Mutailipu, *Adv. Opt. Mater.*, 2025, **13**, 2500631.

43 J. Lu, X. Liu, M. Zhao, X.-B. Deng, K.-X. Shi, Q.-R. Wu, L. Chen and L.-M. Wu, *J. Am. Chem. Soc.*, 2021, **143**, 3647–3654.

44 H. Tian, C. Lin, X. Zhao, S. Fang, H. Li, C. Wang, N. Ye and M. Luo, *Mater. Today Phys.*, 2022, **28**, 100849.

45 H. Yan, Y. Matsushita, K. Yamaura and Y. Tsujimoto, *Angew. Chem., Int. Ed.*, 2021, **60**, 26561.

46 X. Lu, Z. Chen, X. Shi, Q. Jing and M.-H. Lee, *Angew. Chem., Int. Ed.*, 2020, **59**, 17648.

47 L. Wu, C. Lin, H. Tian, Y. Zhou, H. Fan, S. Yang, N. Ye and M. Luo, *Angew. Chem., Int. Ed.*, 2024, **63**, e202315647.

48 A. Tuer, S. Krouglov, R. Cisek, D. Tokarz and V. Barzda, *J. Comput. Chem.*, 2011, **32**, 1128–1134.

49 F. Bu, X. Liu, H. Yu, R. Liu, Z. Hu, J. Wang, Y. Wu and H. Wu, *Inorg. Chem.*, 2024, **63**, 24059–24064.

50 H. Liu, H. Wu, Z. Hu, J. Wang, Y. Wu, P. S. Halasyamani and H. Yu, *ACS Mater. Lett.*, 2023, **5**, 155–161.

51 Q. Wang, W. Song, Y. Lan, L. Cao, L. Huang, D. Gao, J. Bi and G. Zou, *Inorg. Chem. Front.*, 2022, **9**, 3590–3597.